Available online at www.sciencedirect.com
SCIENCE DIRECT®
International Journal of Heat and Mass Transfer 47 (2004) 2989–3001
International Journal of HEAT and MASS TRANSFER
www.elsevier.com/locate/ijhmt

Transport phenomena in an aluminum nitride induction heating sublimation growth system

Bei Wu *, Hui Zhang

Department of Mechanical Engineering, State University of New York at Stony Brook, Stony Brook, NY, 11794-2300, USA

Received 26 June 2003; received in revised form 6 March 2004
Available online 17 April 2004

Abstract

In this paper, an integrated model considering induction heating, thermal system design, mass transport and growth kinetics has been developed to study temperature distribution in an aluminum nitride (AlN) growth system and evolution of the crystal interface and source surface. The electromagnetic field and induction heat generation are calculated by the Maxwell equations. Temperature distribution in the growth chamber is simulated by energy equation accounting for conduction/radiation. Simulation results are in good agreement with experimental measurements. Both of them show that temperature difference between the top and bottom of the crucible is almost independent of power. The effects of RF coil current on temperature distribution is investigated. The maximum temperature is located at about the center of the coils. Effects of pressure and temperature gradient on the growth rate are studied. The growth rate increases linearly with temperature gradient and decreases with pressure. Since the AlN source powder is porous, the effects of the powder porosity on the shapes of the crystal interface and source surface and the growth rate are also investigated.
© 2004 Elsevier Ltd. All rights reserved.

1. Introduction

Due to its high electrical resistivity (10^{10} Ω m), high thermal conductivity (340 W/m K), large band gap (6.28 eV), high acoustic wave velocity and excellent lattice and thermal expansion match with GaN [1], AlN is an attractive candidate for electronic, optical and optoelectronic applications. It can be used to fabricate electronic and optoelectronic devices capable of operation at high temperature, high power and high frequency, such as solar blind UV light detectors, blue light emitting diodes (LEDs), UV laser diodes, and microwave devices [2]. The structure of AlN possesses the same wurzite hexagonal (2H) crystalline structure as that of GaN with a lattice mismatch along the *c*-plane of approximately 2.4%. Also, the thermal expansion coefficient of AlN is smaller than that of GaN at temperature below 300 °C and it is larger at temperature beyond 300 °C. Consequently, the integrated thermal expansion mismatch approaches zero at approximately 1000 °C, and it is highly desirable to avoid cracking of the epitaxial structure during the cooling process in device fabrication [3].

Many groups have worked on growing AlN bulk crystals and improving the crystal quality. AlN crystals are typically produced by sublimation from an AlN source at a temperature above 1800 °C under a nitrogen environment [4,5]. Singh et al. [6] have grown an AlN boule of 25 mm in diameter and 15 mm in length using induction heating sublimation growth process under the conditions of source temperature: 2250 °C, N_2 pressure: 500 Torr and temperature difference between the source and seed surface: 30–90 K. The study has revealed that AlN single crystal boules can possess a high structural quality with dislocation density in the range of 800–1000/cm^2; the distribution of dislocations is inhomogeneous and large areas of the wafer are free from dislocations [7].

In a sublimation growth system, the time-harmonic electromagnetic field induces eddy current in the graphite susceptor that has a high electrical conductivity, and

* Corresponding author. Tel.: +1-631-632-1490; fax: +1-631-632-8544.
E-mail address: bwu@ic.sunysb.edu (B. Wu).

0017-9310/$ - see front matter © 2004 Elsevier Ltd. All rights reserved.
doi:10.1016/j.ijheatmasstransfer.2004.03.001

Nomenclature

A_{AlN}	growth area (m^2)
A_{gas}	evaporation area (m^2)
A	constant in Eqs. (10) and (17)
A_0	magnetic vector potential (Wb/m)
A_r	in-phase component, real part (Wb/m)
A_i	out-phase component, imaginary part (Wb/m)
B	constant in Eqs. (10) and (17)
c	constant in Eq. (17)
c_p	isobaric specific heat (J/kg K)
d	diameter of crucible (m)
d_p	average particle diameter of AlN powder
D	diffusion coefficient (m^2/s)
F	dimensionless rotational frequency, fd^2/v
f	frequency (Hz)
$F_{j,k}$	view factor
g	gravitational acceleration (m/s^2)
Gr	Grashof number, $\rho^2 g\beta L^3 \Delta T/\mu^2$
ΔG	free energy (J/mol)
ΔH	enthalpy (J/mol)
ΔH_{vs}	latent heat (J/mol)
J_0	current density (A/m^2)
J_{Al}	Mole flux of Al vapor (mol/m^2 s)
k	thermal conductivity (W/m K)
K_p	equilibrium constant
L	distance between the source and seed (m)
M	molecular weight
P	pressure (Pa)
P^*_{Al}	"thermodynamic" partial pressure (Pa)
Pe	mass Péclet number, UL/D
Pr	Prandtl number, $\mu c_p/k$
Q	heat (W)
q'''	heat power by eddy current (W/m^3)
q''	radiative heat flux (W/m^2)
r	radial coordinate (m)
R	universal gas constant, 8.314 (J/mol K)
R_d	resistance of mass diffusion (kg/m mol)
R_k	kinetic resistance (kg/m mol)
s	stoichiometric factor
ΔS	entropy (J/K mol)
t	time (s)
T	temperature (K)
ΔT	temperature difference between the source and seed (K)
U	gas velocity (m/s)
V_g	growth rate (mm/h)
z	axial coordinate (m)

Greek symbols

α	absorptivity, sticking coefficient
β	isobaric expansion coefficient (1/K)
ε	emissivity
ε_m	permittivity (F/m)
ε_p	porosity
μ	viscosity (kg/m s)
μ_m	magnetic permeability, $4\pi \times 10^{-7}$ (H/m)
v	kinematic viscosity, μ/ρ (m^2/s)
ρ	density (kg/m^3)
σ_c	electrical conductivity ($1/\Omega$ m)
σ	Stefan–Boltzmann constant ($W/m^2 K^4$)
ω	angular frequency of the AC current (rad/s)

Subscripts

Al	aluminum
AlN	aluminum nitride
avg	average
coil	induction coil
eddy	eddy currents
eff	effective
insu	insulation material
latent	latent heat related parameter
N_2	nitrogen
radi	radiative
real	real part of complex quantity
seed	seed interface
source	source material
Stefan	Stefan flow related
total	total pressure

heat is generated by the RF coils following Joule's law. The growth process consists of several steps: sublimation of source material, transport in the gas phase, impingement of atoms at the seed surface, surface diffusion, and surface adsorption/desorption. The analysis of the vapor deposition at the growth interface includes the understanding of thermodynamics, mass transport, and surface kinetics phenomena [8]. Thermodynamic study of the phase equilibria during vapor growth provides a basic understanding of the process. The feasibility of reaction, the composition and amount of the solid and gaseous species presence in the growth system can be determined from the calculation of thermodynamic equilibrium at a given set of processing conditions such as deposition temperature, pressure and reactant concentration. Thermodynamics analysis will provide maximum growth rate. The surface kinetics is the most challenging task as it involves the crystalline structure of the material, supersaturation, atom stickiness and movement on the surface. Kinetic Monte Carlo simulation is needed to accurately predict the deposition rate for this case. The overall growth rate is limited by the slowest reaction step [9]. The transport of growth species from the source to the growing interface is often the

rate-limiting step in sublimation vapor growth process. The understanding of the vapor transport and the interplay between vapor transport and surface kinetics is important for the optimization of the sublimation growth process.

Numerical simulation has been widely used to study the vapor growth process because of the difficulty in in-situ measurements. A multidimensional model was developed and used to simulate the chemical vapor deposition (CVD) of silicon nitride in a low-pressure hot-wall reactor by Evans and Greif [10]. Irreversible surface reactions were used to model the deposition chemistry. They found that except for the high flow rate conditions, significant upstream diffusion occurs, resulting in dilution of the reactants [10]. A finite-volume model has been developed to study gas flow and heat transfer of an optical fiber as it travels through a CVD reactor by Iwanik and Chiu [11]. The study showed that the draw speed significantly affected the fiber temperature inside the reactor. Other parameters affecting fiber temperature included fiber radius, fiber coating emissivity, and gas flow velocity at the inlet [11]. Yoo and Jaluria [12] studied the continuous chemical vapor deposition of silicon in a horizontal cold wall reactor and paid special attention to a moving susceptor. A two-dimensional numerical model that accounted for variable properties, thermal diffusion, radiative heat exchange among surfaces, and conjugate heat transfer between the gas and susceptor was developed and validated. They found that the stationary deposition efficiency was determined by the conductance ratio when the susceptor was motionless. The efficiency monotonically decreases as the ratio increases. When the susceptor was in motion, the deposition efficiency was a function of the susceptor parameter. Numerical simulation was also used to investigate transient behavior during sublimation growth of SiC by physical vapor transport (PVT) [13]. The simulations were based on a transient model for heat transport, together with radio frequency (RF) induction heating. Temperature distributions for different heating powers and induction coil positions were presented.

In this paper, we will utilize the knowledge we have learned on modeling of PVT/CVD growth processes to design an AlN vapor growth system. The order of the magnitude analysis will be performed to determine the primary parameters that control the process. A thermal model will be developed and used to design an induction heating sublimation system for bulk AlN crystal growth. The transport of growth species from the source to the growing interface will be investigated and the growth model will be provided. An integrated heat transfer and growth kinetics model will be developed to predict the growth rate and the evolution of the AlN growth interface for various operating conditions.

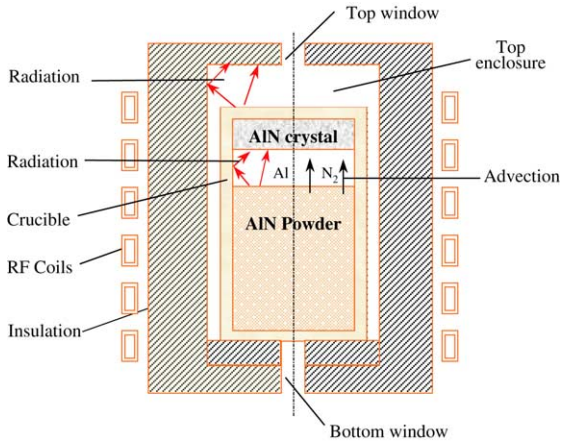

Fig. 1. Schematic of an induction heating sublimation growth system.

2. Experimental setup

The growth experiments are usually performed in the radio frequency (RF) induction heated sublimation reactor. Fig. 1 shows the schematic of an induction heating sublimation growth system. The powder source sublimes at the hot part—the bottom of the crucible, and the gaseous species are then transported to the cool part of the crucible—the cap where the crystal grows by re-crystallization. Cylindrical crucible, made of graphite, with the inner diameter of 1″ and the height of ~2.5″ is used in the growth experiments. A short axial distance between the source and the seed is used to increase the vapor transport and decrease the buoyancy convection effect. Temperature in the growth system can be changed by adjusting the power level and the temperature difference between the source and the seed surface can be modified by adjusting the position of the coils.

The growth experiments were performed in North Carolina State University (NCSU) in temperature range from 1800 to 2400 °C, temperature difference between the top and the bottom of the crucible from 30 to 120 °C, pressure from 400 to 800 Torr, ultra-high purity (UHP) nitrogen flow rate of 100 sccm, and run times from 16 to 50 h. Since the growth process is taken place under a nitrogen environment, the reacting gas in the gap between the source and seed is made up mainly by N_2.

3. Scale analysis

The order-of-magnitude study is presented here to provide basic understanding of the complex thermal transport phenomena in the AlN growth system. The strength of buoyancy flow is quantified by the Grashof

number, $Gr = \frac{\rho^2 g\beta L^3 \Delta T}{\mu^2} = \frac{\rho^2 g L^3}{\mu^2}\frac{\Delta T}{T}$, and the Prandtl number, $Pr = \frac{\mu c_p}{k}$.

The typical growth conditions include that the growth temperature is 2400 K, the temperature difference between the AlN source surface and growth interface is about 30 K, the inner crucible diameter is 25 mm and the distance between the source surface and growth interface is 10 mm for the induction heating AlN sublimation growth system developed in NCSU. The Prandtl number is evaluated as 0.45, and the Grashof number is 10.47 based on the reference length scale of the inner crucible diameter. The value of $Gr = 10.47$ is below the threshold at which natural convection can be considered important.

For the vapor crystal growth, rotation may be used as a control parameter for the growth of high quality crystals. The dimensionless rotational frequency $F = fd^2/v$ is used to define the importance of the rotation. The calculation results are presented in Table 1. From the open literature [14], when $Gr^{1/2}/F$ decreases, i.e. the rotation rate increases, the growth rates tend to decrease, meanwhile the morphology stability is improved. When $Gr^{1/2}/F$ reaches a critical number about 3.3–5.5 [14], the growth rate becomes saturate. Based on the critical number of $Gr^{1/2}/F = 4.43$, the optimal rotation rate is estimated around 30 rpm (see Table 1). If the rotation rate is greater than 30 rpm, even though the morphology might be improved, the growth rate will decrease. On the other hand, if the rotation rate is less than 30 rpm, the growth rate remains unchanged, the morphology may, however, become worse. Since no experimental data is available for AlN rotation growth, we use the data from [14], in which the vapor deposition of ZnSe in a rotating horizontal growth reactor is studied. It should be noted that the critical number may not be the same for the case of AlN growth. It can, however, be concluded that the rotation is an important control parameter for the AlN growth process.

Another important issue being addressed is the effect of the Stefan flow on mass transport and global heat transfer. If the only movement assumed inside the gap between the source and seed is the transport of Al vapor and N_2 from the source to the seed, the magnitude of the advective velocity, induced by the sublimation of AlN, can be estimated from the growth rate

$$U = \rho_{\mathrm{AlN}} V_{\mathrm{g}} A_{\mathrm{AlN}} / \rho_{\mathrm{N2}} A_{\mathrm{gas}}, \tag{1}$$

where U denotes the gas velocity and ρ_{N2} is the density of nitrogen gas calculated by the ideal gas law. This leads to the Péclet number for mass transfer

$$Pe = UL/D, \tag{2}$$

where the diffusion coefficient D is obtained from Liu and Edgar [15]

$$D = D_0 (T/T_0)^n (P_0/P), \tag{3}$$

where $D_0 = 5 \times 10^{-6} \sim 2 \times 10^{-4}$ m^2/s, $n = 1.8$, $T_0 = 300$ K, $P_0 = 1$ atm $= 760$ Torr. Combining Eqs. (1)–(3) together with ideal gas law $\rho_{\mathrm{N2}} = PM/RT$, the Péclet number can be rewritten as

$$Pe = \frac{\rho_{\mathrm{AlN}} V_{\mathrm{g}} L R T_0^n}{D_0 M_{\mathrm{N_2}} T^{n-1} P_0} \tag{4}$$

with the assumption of $A_{\mathrm{AlN}} = A_{\mathrm{gas}}$. It is interesting to know that the Péclet number is independent of the gas pressure, P. Using $D_0 = 1 \times 10^{-5}$ m^2/s, $T_0 = 300$ K, $P_0 = 1$ atm and $L = 10$ mm for the induction heating system, the Péclet number at the growth temperature from 2100 to 2700 K are summarized in Table 2 for a given growth rate of 1.0 mm/h, which is the growth rate recently achieved in NCSU. The value of the Péclet number indicated that the Stefan flow may be important for AlN growth at a high growth rate.

If the buoyancy effect is neglected, the energy exchange in the gap between the source and seed is governed by radiative heat transfer, Stefan flow (advective mass transport), and latent heat released during deposition (or absorbed during sublimation). The amount of heat transferred by these three modes can be estimated as

$$Q_{\mathrm{latent}} = \rho_{\mathrm{AlN}} V_{\mathrm{g}} A_{\mathrm{AlN}} \Delta H_{\mathrm{vs}}, \tag{5a}$$

$$Q_{\mathrm{Stefan}} = \rho_{\mathrm{AlN}} V_{\mathrm{g}} A_{\mathrm{AlN}} c_p \Delta T, \tag{5b}$$

$$Q_{\mathrm{radi}} = \varepsilon A_{\mathrm{AlN}} \sigma (T_{\mathrm{source}}^4 - T_{\mathrm{seed}}^4). \tag{5c}$$

For a growth rate of $V_{\mathrm{g}} = 1.0$ mm/h, a crucible diameter $d = 25$ mm, $\Delta T = 40$ K, $\varepsilon = 0.8$, $T_{\mathrm{seed}} = 2400$ K, and

Table 1
Scaling analysis on rotational effects

T (K)		2400	
ΔT (K)		30	
d (mm)		25	
RPM	20	30	60
F	0.487	0.7304	1.461
Gr		10.47	
$Gr^{1/2}/F$	6.64	4.43	2.21

Table 2
Péclet number for different temperatures with the growth rate of 1 mm/hour

Temperature (K)	Pe
2100	0.167
2200	0.161
2300	0.156
2400	0.150
2500	0.146
2600	0.141
2700	0.137

$\Delta H_{vs} = 630.1$ KJ/mol [15]. The results of Q_{latent}, Q_{Stefan} and Q_{radi} are 6.81, 0.023 and 50.49 W, respectively. Q_{Stefan} is much smaller than Q_{radi}. It is, therefore, reasonable to neglect the heat transfer by Stefan flow in modeling of the global temperature distribution. It has also been commonly assumed that chemical reactions, both exothermic and endothermic, will not contribute significantly to heat transfer and temperature distribution in the AlN growth system.

4. Mathematical model of induction heating system

An induction heated AlN bulk sublimation growth system has been simulated in this paper. Fig. 1 is the schematic of an induction heating sublimation growth system. The electromagnetic field and Joule's heat produced by the induction heating coils are calculated by the Maxwell equations, and the transient temperature distribution in the growth chamber is simulated by energy equation accounting for the conduction and radiation within and between various components.

The azimuthal component A_0 ($A_0 = A_r + iA_i$) of the magnetic vector potential is solved for induction heating coils. The Maxwell equations in terms of A_r and A_i can be written as follows [16,17]:

$$\left(\frac{\partial^2}{\partial r^2}+\frac{1}{r}\frac{\partial}{\partial r}-\frac{1}{r^2}+\frac{\partial^2}{\partial z^2}\right)\left(\frac{A_r}{\mu_m}\right)+\varepsilon_m\omega^2 A_r+\omega\sigma_c A_i = -J_0, \tag{6a}$$

$$\left(\frac{\partial^2}{\partial r^2}+\frac{1}{r}\frac{\partial}{\partial r}-\frac{1}{r^2}+\frac{\partial^2}{\partial z^2}\right)\left(\frac{A_i}{\mu_m}\right)+\varepsilon_m\omega^2 A_i-\omega\sigma_c A_r = 0, \tag{6b}$$

where the real part A_r is referred as the in-phase component and the imaginary part A_i is termed as the out-of-phase component, and J_0 is the current density in the azimuthal direction in the induction heating coils.

It is assumed that the contribution of convective heat transfer inside the gas phase is negligible. The energy transport equation can be written as follows:

$$(\rho c_p)_{\text{eff}}\frac{\partial T}{\partial t} = \nabla\cdot(k_{\text{eff}}\nabla T)+q'''_{\text{eddy}}+q'''_{\text{latent}}+\nabla\cdot q''_{\text{radi}}, \tag{7a}$$

where q''_{radi} represents the radiative heat flux on the surfaces of inner enclosure. The generated heat by the eddy current in the graphite susceptor can be expressed as $q'''_{\text{eddy}} = \frac{1}{2}\sigma_c\omega^2(A_r^2+A_i^2)$. The effective heat capacity $(\rho c_p)_{\text{eff}}$ and thermal conductivity k_{eff} for the porous medium are estimated from

$$(\rho c_p)_{\text{eff}} = \varepsilon_p(\rho c_p)_{\text{gas}}+(1-\varepsilon_p)(\rho c_p)_{\text{solid}}, \tag{7b}$$

$$k_{\text{eff}} = \varepsilon_p\left(k_{\text{gas}}+\frac{32}{3}\varepsilon\sigma T^3 d_p\right)+(1-\varepsilon_p)k_{\text{solid}}, \tag{7c}$$

where $0 \leqslant \varepsilon_p < 1$ is the porosity of the AlN powder and d_p is the average particle diameter of the powder [18]. Within a non-porous solid or the gas, $(\rho c_p)_{\text{eff}}$ and k_{eff} are the heat capacity and thermal conductivity of the solid or the gas, respectively.

In the radiation model, the nitrogen gas and vapor species are considered as fully transparent, and all the surfaces are grey, opaque and diffusive. The grid-to-grid gray-diffusive method requires the faces in the computational domain to be divided into grids. The radiation surfaces are thus divided into a number of rings, each with uniform properties. The rings coincide with the grids defined in the curvilinear finite volume method, and the view factors between each pair of rings are calculated. The total exchange factor method will be used to relate the temperature at the grid with the heat flux q''_{radi} [19], while q''_{radi} is calculated by solving the following radiation equation for grey and diffuse surfaces [20]

$$\frac{q''_{\text{radi},j}}{\varepsilon_j}-\sum_{k=1}^{N}F_{j,k}\frac{1-\varepsilon_k}{\varepsilon_k}q''_{\text{radi},k} = \sigma T_j^4-\sum_{k=1}^{N}F_{j,k}\sigma T_k^4, \tag{8}$$

where $F_{j,k}$ is the view factor from ring j to ring k, and ε is the emissivity of radiative surface. The electromagnetic and energy equations are solved by using an in-house developed software [16,17,21].

5. Growth model

For the AlN sublimation crystal growth, the following reaction is considered:

$$\text{Al(g)}+\frac{1}{2}\text{N}_2\text{(g)} \leftrightarrow \text{AlN(s)}. \tag{9}$$

Table 3
Order-of-magnitude analysis of kinetic resistance and diffusion resistance

Average temperature (K)	R_k	R_d
2000	106.22	2.88×10^5
2200	111.41	2.67×10^5
2400	116.36	2.49×10^5
2600	121.11	2.33×10^5

Table 4
Thermophysical properties used in the analysis and modeling

Properties	AlN	N_2 (at 2000 °C, 1 atm)
Specific heat (J/kg K)	1080	1297
Density (kg/m^3)	3250	0.1502
Thermal conductivity (W/m K)	220	0.1859
Viscosity (kg/m s)	–	642.6×10^{-7}
Kinematic viscosity (m^2/s)	–	427.8×10^{-6}

For the reversible reaction (9), the "thermodynamic" partial pressures of aluminum vapor and nitrogen gas satisfy [15]

$$P^*_{\mathrm{Al}}(P^*_{\mathrm{N_2}})^{1/2} = K_p = \exp\left(-\frac{\Delta G}{RT}\right) = \exp\left(\frac{\Delta S}{R} - \frac{\Delta H}{RT}\right) = \exp\left(A - \frac{B}{T}\right). \quad (10)$$

The parameters in Eq. (10) can be calculated according to the thermodynamics data, $A = 27.055$ and $B = 75788$ [15].

The dissociation of AlN source material happens on the source surface. The mole flux of the aluminum vapor at the source surface can be estimated by the Hertz–Knudsen model

$$J_{\mathrm{Al}} = \frac{\alpha_{\mathrm{Al}}[P^*_{\mathrm{Al,source}} - P_{\mathrm{Al,source}}]}{\sqrt{2\pi M_{\mathrm{Al}} RT}}, \quad (11a)$$

where P_{Al} is the Al vapor pressure at the source interface. M_{Al} is the molecular weight of Al. α_{Al} is the sticking coefficient of Al on AlN source and growth surface. $\alpha_{\mathrm{Al}} = 1$ is used in this paper [22]. The transport rate from vapor to solid phases at the growth interface is related to supersaturation at the growth interface by the Hertz–Knudsen model

$$J_{\mathrm{Al}} = \frac{\alpha_{\mathrm{Al}}[P_{\mathrm{Al,seed}} - P^*_{\mathrm{Al,seed}}]}{\sqrt{2\pi M_{\mathrm{Al}} RT}}. \quad (11b)$$

If the mass transport is driven by the pressure difference between the source and seed ends, the rate of mass transport for Al vapor can be calculated from

$$J_{\mathrm{Al}} = \frac{P_{\mathrm{Al,souce}} - P_{\mathrm{Al,seed}}}{LRT_{\mathrm{avg}}/D}. \quad (11c)$$

For the steady-state case, three mole fluxes in Eqs. (11a)–(11c) are equal to each other. Based on the network concept in heat conduction, the following expression can be obtained by combining Eqs. (11a), (11b) and (11c) to predict the mole flux J_{Al}:

$$J_{\mathrm{Al}} = \frac{P^*_{\mathrm{Al,source}} - P^*_{\mathrm{Al,seed}}}{\sqrt{2\pi M_{\mathrm{Al}} RT_{\mathrm{source}}}/\alpha_{\mathrm{Al}} + LRT_{\mathrm{avg}}/D + \sqrt{2\pi M_{\mathrm{Al}} RT_{\mathrm{seed}}}/\alpha_{\mathrm{Al}}}. \quad (12)$$

Since $J_{\mathrm{Al}} = J_{\mathrm{AlN}}$, the growth rate V_{g} can then be expressed as

$$V_{\mathrm{g}} = \frac{M_{\mathrm{AlN}}}{\rho_{\mathrm{AlN}}} J_{\mathrm{AlN}} = \frac{M_{\mathrm{AlN}}}{\rho_{\mathrm{AlN}}} J_{\mathrm{Al}}. \quad (13)$$

The summation of $\sqrt{2\pi RM_{\mathrm{Al}}T_{\mathrm{source}}}$ and $\sqrt{2\pi RM_{\mathrm{Al}}T_{\mathrm{seed}}}$ represents the kinetic resistance at the source and seed surfaces, denoted by R_k; LRT/D represents the resistance of mass diffusion, denoted by R_{d}. The following expression can be obtained:

$$R_{k,\mathrm{source}} = \sqrt{2\pi RM_{\mathrm{Al}}T_{\mathrm{source}}},$$
$$R_{k,\mathrm{seed}} = \sqrt{2\pi RM_{\mathrm{Al}}T_{\mathrm{seed}}},$$
$$R_{\mathrm{d}} = LRT/D = LRT_{\mathrm{avg}}/D, \quad (14)$$

where $T_{\mathrm{avg}} = (T_{\mathrm{source}} + T_{\mathrm{seed}})/2$ and D is the diffusion coefficient defined in Eq. (3) with $D_0 = 1 \times 10^{-5}$ m^2/s. For a typical operating pressure $P = 400$ Torr, $L = 10$ mm, the order-of-magnitude analysis has been carried out to examine the significance of the growth kinetics and mass transport in a temperature range from 2000 to 2600 K (see Table 3). Due to temperature difference between the charge surface and the seed surface is usually less than 100 K, R_k can be approximated by $2\sqrt{2\pi RM_{\mathrm{Al}}T_{\mathrm{avg}}}$. It is seen in Table 3 that the kinetic resistance is much smaller than the diffusion resistance for the pressure of 400 Torr. It may be concluded that the kinetic resistance at the source or seed plays a minor role at medium and high pressures, and it is therefore reasonable to neglect R_k in the mole flux equation.

In the open literature [15], the supersaturation at the surfaces for the high pressure case (>200 Torr) is really low and can therefore be neglected. The mass transport is dominated by the Stefan flow. If the process can be approximated by a one-dimensional model, the following formulation for mole flux is proposed considering the Stefan flow [15]:

$$J_{\mathrm{Al}} = \frac{DP_{\mathrm{total}}}{RTsL} \ln\left(\frac{P_{\mathrm{total}}/s - P_{\mathrm{Al,seed}}}{P_{\mathrm{total}}/s - P_{\mathrm{Al,source}}}\right), \quad (15)$$

where s is the stoichiometric factor which is equal to 3/2 in this case. An approximation can be derived at conditions that the system pressure is sufficient high and the temperature difference is small, e.g. $P_{\mathrm{Al}} \ll P_{\mathrm{total}} \approx P_{\mathrm{N_2}}$, the mole flux at the surface can be expressed as

$$J_{\mathrm{Al}} = \frac{DP_{\mathrm{total}}}{RT_{\mathrm{avg}}sL} \ln\left(1 + \frac{P_{\mathrm{Al,source}} - P_{\mathrm{Al,seed}}}{P_{\mathrm{total}}/s - P_{\mathrm{Al,source}}}\right) \cong \frac{DP_{\mathrm{total}}}{RT_{\mathrm{avg}}sL} \cdot \frac{P_{\mathrm{Al,source}} - P_{\mathrm{Al,seed}}}{P_{\mathrm{total}}/s - P_{\mathrm{Al,source}}} = \frac{D}{RT_{\mathrm{avg}}L} \cdot [P_{\mathrm{Al,source}} - P_{\mathrm{Al,seed}}]. \quad (16)$$

A linear relation of Eq. (11c) has been resolved, which means that at the high pressure case, the Stefan flow controlled flux rate is the same as the diffusion controlled one. Combining Eqs. (16) and (10), the final expression of the growth rate can be expressed as:

$$V_{\mathrm{g}} = c\frac{\exp(A - B/T)}{P^{1.5}T^{1.2}}\frac{\Delta T}{L}, \quad (17)$$

where $c \cong 407.54$ by interpolating the experimental data in Liu and Edgar [15]. All the thermal properties used in calculations and simulations are listed in Table 4 [23].

6. Results and discussion

Fig. 2(a) shows the distributions of in-phase (A_r) and out-of-phase (A_i) components at the current of 980 A and frequency of 10 kHz designed for the growth system in NCSU. The top of the coils is lower than the top insulation disk by 1.3 in. The in-phase component has the maximum value around the coils, and the contour shape is obviously influenced by the geometry of the coils, while the maximum absolute value of the out-of-phase component concentrates in the graphite crucible. Interestingly, their absolute values are about the same

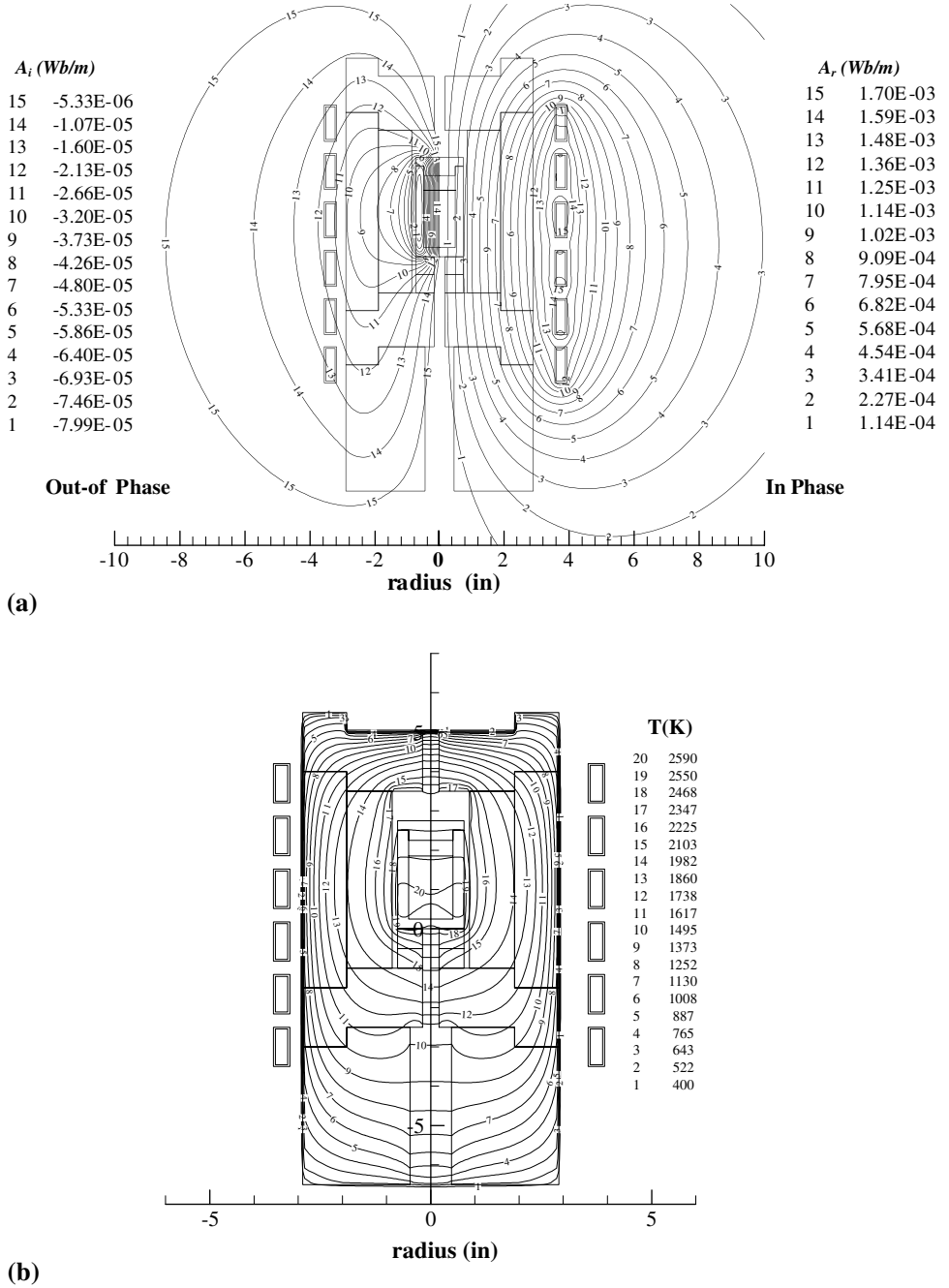

Fig. 2. (a) Electromagnetic field distribution and (b) temperature distribution in the AlN growth system in NCSU.

order of the magnitude in the crucible. Therefore, both in-phase and out-of-phase components need to be considered in the heat generation.

Because of the axial position of the coils, the bottom part of the crucible produces more heat than the top part. The temperature distribution in the entire growth system after it reaches quasi-steady state is presented in Fig. 2(b). The highest temperature takes place at the lower part in the crucible wall, whose axial position corresponds to the center of the induction coils. The temperature difference between the source surface and crucible lid is about 40 K. The radial temperature difference between the center and periphery is very small (<10 K). The explanation is that the diameter of the system is small and a top enclosure located above the crucible (see Fig. 1) acts as a black hole for radiation. The axial temperature gradient is closely related to the axial position of the coil and the diameter of the top window size, from which heat is transferred out of the chamber.

Fig. 3(a) is the comparison between the experimental and simulation results. The dashed and dash-dotted lines are the top and bottom temperatures measured by optical pyrometers from the top and bottom windows. The symbols are the simulation results for the current density of 800, 900 and 980 A, respectively. The frequency used in all three cases is 10 kHz. The simulation results match well with experiments. Both the experimental and simulation results show that the temperature difference between the top and bottom of the crucible is almost independent of power. Fig. 3(b)–(d) are the temperature distributions within the crucible for 800, 900 and 980 A, respectively. The maximum temperature appears in the graphite crucible, and is always located at about the geometric center of the induction coil. In the source powder, the maximum temperature is at the

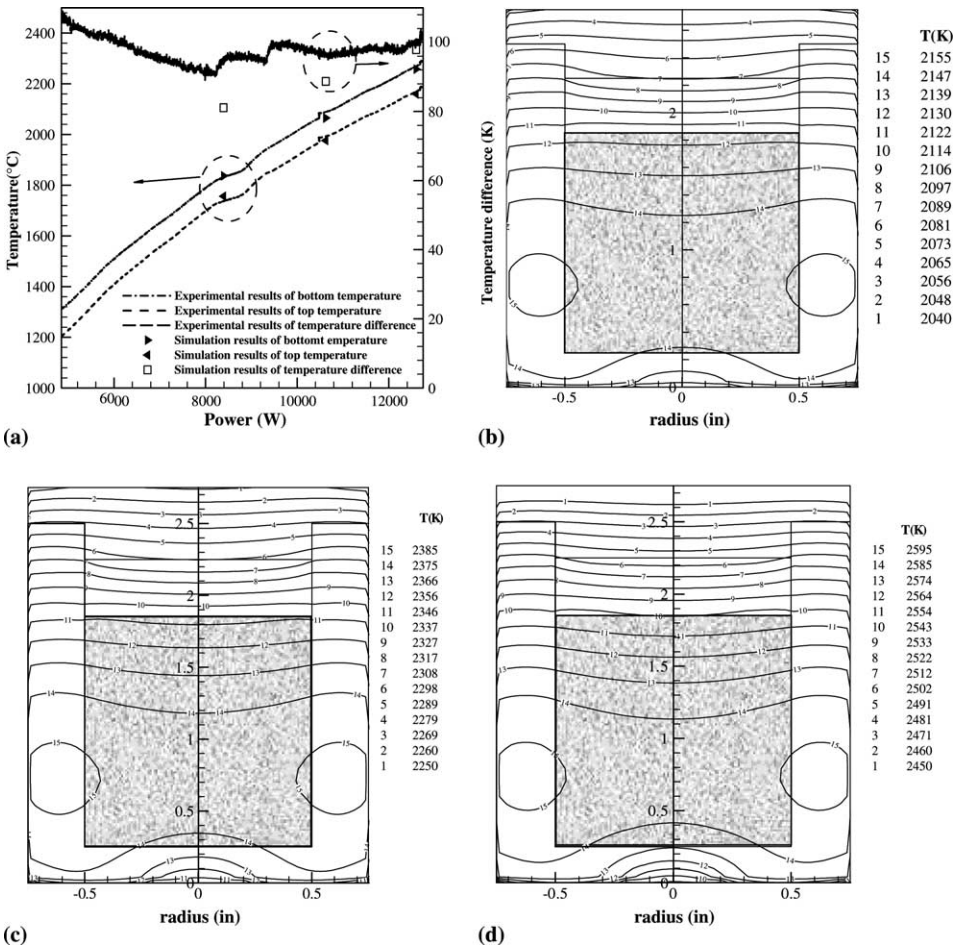

Fig. 3. (a) The top and bottom temperature and the temperature difference as a function of heating power in an AlN growth system in NCSU; temperature distributions in the crucible with current density of (b) 800 A; (c) 900 A and (d) 980 A, respectively.

lower middle portion near the crucible wall. The positive temperature difference between the AlN source surface and the crucible lid allows the sublimation of AlN powder in the source and deposition of AlN on lid. As shown in Fig. 3, the temperature has a slightly lower value at the center of the lid because of the cooling effect due to the presence of the top window. The lower temperature at the center of the lid ensures a convex shape of the crystal interface, which benefits to defect reduction.

Fig. 4(a) and (b) is the temperature profiles along the axial and radial directions with different current densities. The center-line temperature profiles (Fig. 4a) reveal that the temperature difference between the top and bottom of the crucible will vary slightly with the heating power. For the current of 980 A, the calculation results without radiation between the source and seed is also presented. The result is very different from that predicted considering radiation. It can be concluded that radiation inside the growth cell is very strong and has to be included in the model. The maximum temperature is located inside the AlN source powder along the center line, which is decided by the coil position. Fig. 4(b) shows that temperature along the crucible lid is quite uniform.

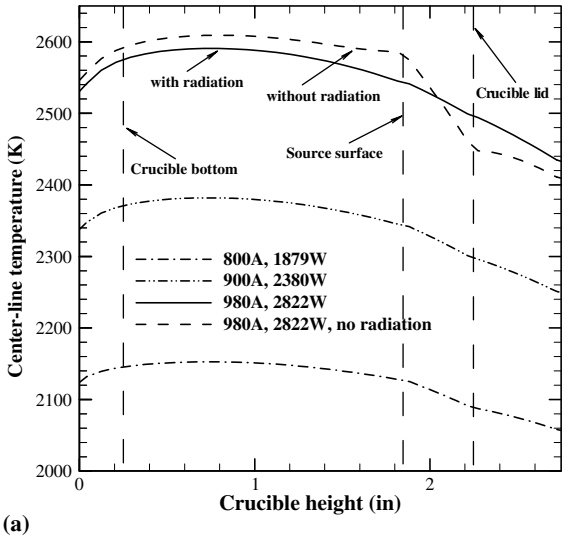

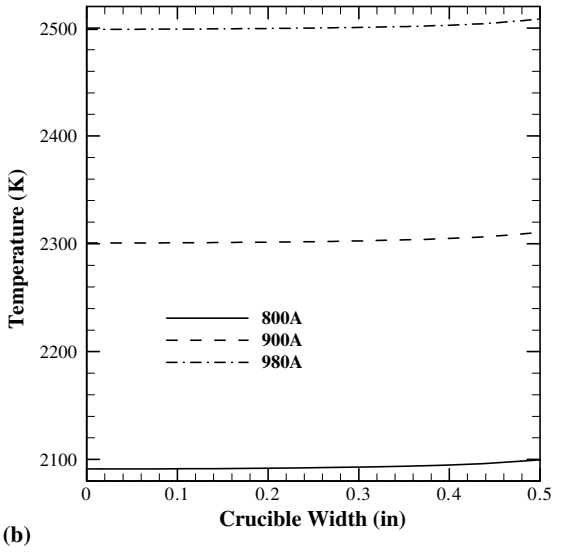

Fig. 4. (a) Axial temperature distribution in the crucible; (b) radial temperature distribution in the crucible.

Fig. 5(a) and (b) shows the temperature distributions in the crucible for the current of 980 A and the distance from the source surface to the crucible lid is varied from 20 mm and 30 mm, which are two or three times as the original in Fig. 3(d). Fig. 5(c) shows the temperature of crucible lid and source surface when the distance changes from 10 to 30 mm. With the increase of the distance, the temperature difference increases from 47 to 63 K. On the other hand, the temperature gradient decreases from 4.7 to 2.1 K/mm. The growth rate as a function of average temperature is presented in Fig. 6. The growth rate increases exponentially with temperature and linearly with temperature gradient; and it decreases with pressure.

In this paper, the effects of the powder porosity on the growth process are also investigated. To satisfy the mass conservation, the mass of the as-grown crystal should equal to the powder consumption. We assume that the source material will evaporate from the top surface. Fig. 7 shows the predicted crystal and source shapes at different time for $\varepsilon_p = 0.2$. Due to the porous powder, the distance between the crystal and powder surface increases, and the growth rate decreases with the process time. Along the radial direction, the temperature on the crucible wall is higher than that at the center (see Figs. 3 and 4), therefore, the powder near the crucible wall evaporates earlier than that at the center. Consequently, the growth rate in the center portion is higher than that near the wall. Fig. 8(a) and (b) shows the predicted crystal and source interface shapes after 10 h for different porosities. With the larger porosity, the crystal growth rate is smaller; meanwhile more powder will be consumed during the growth. Fig. 8(c) shows that the average growth rate decreases with the process time. The porosity will not affect the growth rate significantly at this condition. For the larger porosity, the growth rate is only slightly smaller because of the larger distance between the source surface and growth interface. The calculation results are in the same range with the experimental data. Fig. 8(d) demonstrates the crystal interface shapes when the growth process is terminated for different porosities. It is interesting to find out that the growth will stop at different time for different reasons. For the solid powder ($\varepsilon_p = 0$), the growth will stop after 13 h growth because of the center portion of the

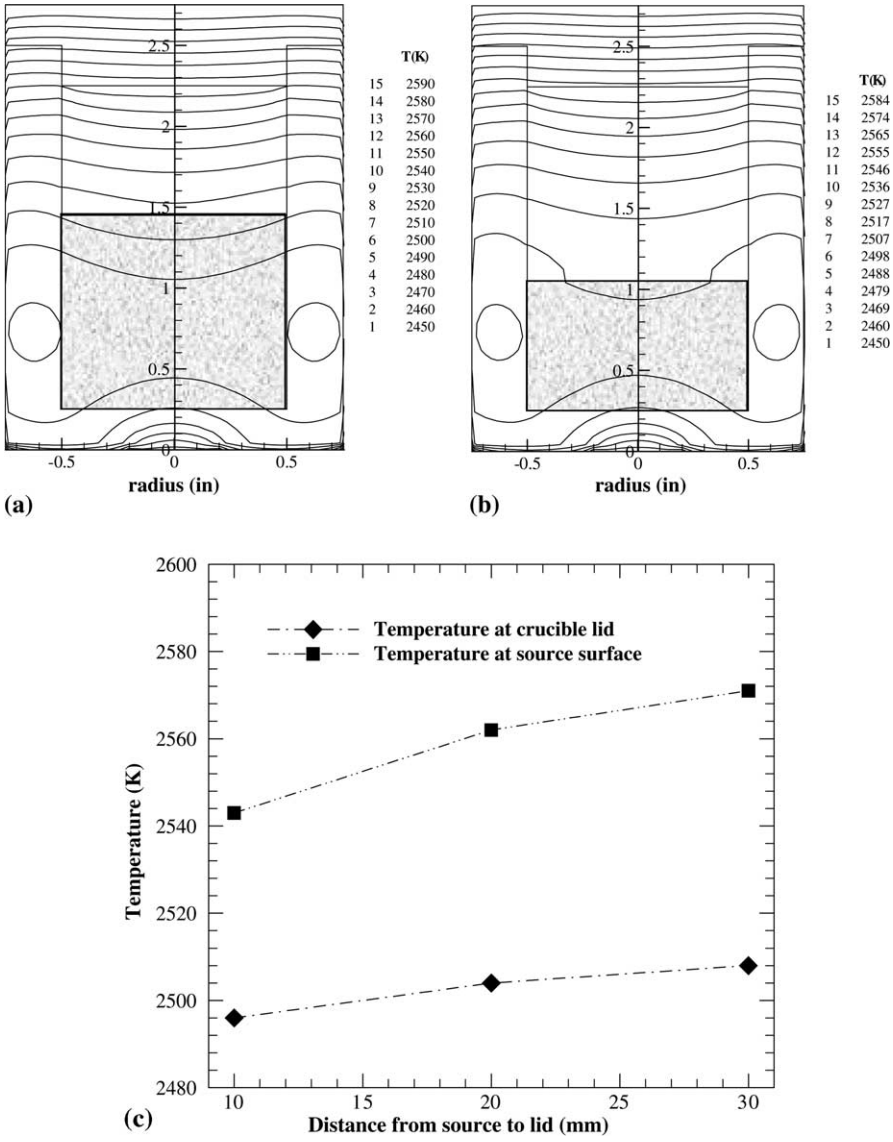

Fig. 5. Temperature distribution in the crucible with the current of 980 A and distance between source surface and lid of: (a) 20 mm; (b) 30 mm, respectively and (c) source surface and lid bottom temperature for different source-lid distances.

crystal will reach the top surface of the powder. For $\varepsilon_p = 0.2$, the growth will be after 20 h, since the temperature at the crystal interface at this time equals to that at the power surface. For $\varepsilon_p = 0.4$, the crystal growth will be terminated after 18 h because all powders are consumed.

7. Conclusions

The order of the magnitude analysis is performed to understand transport phenomena in an AlN sublimation growth system. A comprehensive process model for aluminum nitride vapor growth has been developed that accounts for induction heating, heat and mass transfer, and growth kinetics. The model has been successfully applied to the AlN sublimation growth.

The temperature distribution is predicted for a sublimation growth system. The dependence of temperature distribution on RF coil current has been demonstrated by the numerical results. The simulation results are in good agreement with the experimental data. The results show that the temperature difference between the top and bottom of the crucible is virtually independent of the heating power.

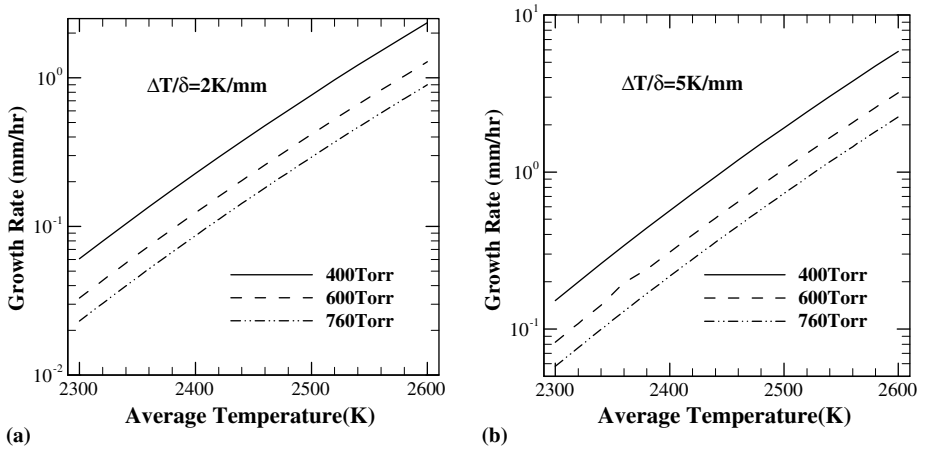

Fig. 6. Growth rates at different pressure and temperature for temperature gradient of: (a) 2 K/mm and (b) 5 K/mm.

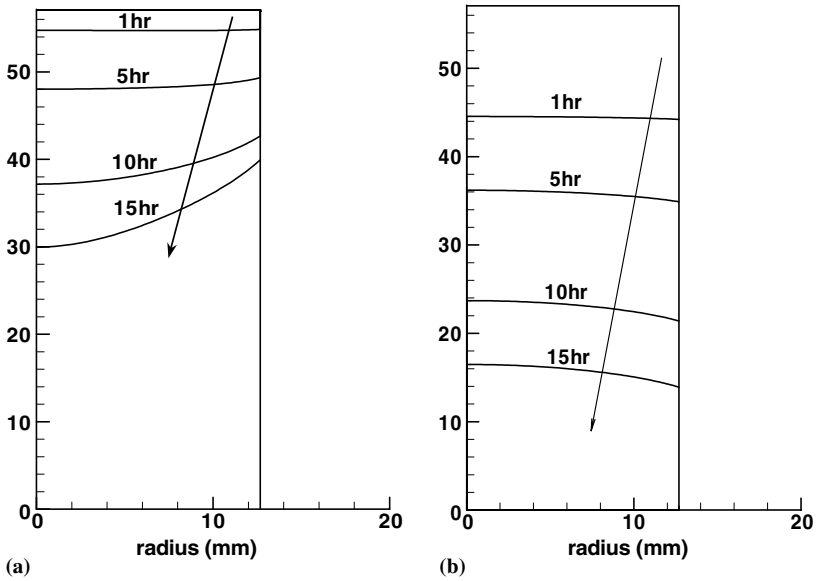

Fig. 7. (a) Crystal interface shapes at different time with $\varepsilon_p = 0.2$ and (b) top surface shape of the powder at different time with $\varepsilon_p = 0.2$.

A growth rate formulation has been proposed and used to examine the effects of temperature, temperature gradient and pressure. When the distance between the source surface and the lid bottom is changed from 10 to 30 mm, the temperature gradient changed from 4.7 to 2.1 K/mm. The growth rate is larger for a smaller gap between the source surface and the lid bottom.

The effects of the powder porosity on the growth process have also been investigated. The crystal growth rate is smaller for a larger porosity. The crystal growth for different powder porosities will be terminated at different time for different reasons. The predicted growth rate is in the same level as the experimental data.

Acknowledgements

We would like to acknowledge the sponsorship of this research by NSF Career award (CTS-9876198) and the DoD Multidisciplinary University Research Initiative (MURI) program administered by the Office of Naval Research under Grant N00014-01-1-1-0716; Dr. Colin E. Wood project monitor. We would also like to acknowledge Mr. Vlado Noveski, Dr. Raoul Schlesser and Dr. Zlatko Sitar from North Carolina State University for providing experimental data and Dr. Ronghui Ma from SUNY at Stony Brook on valuable discussion.

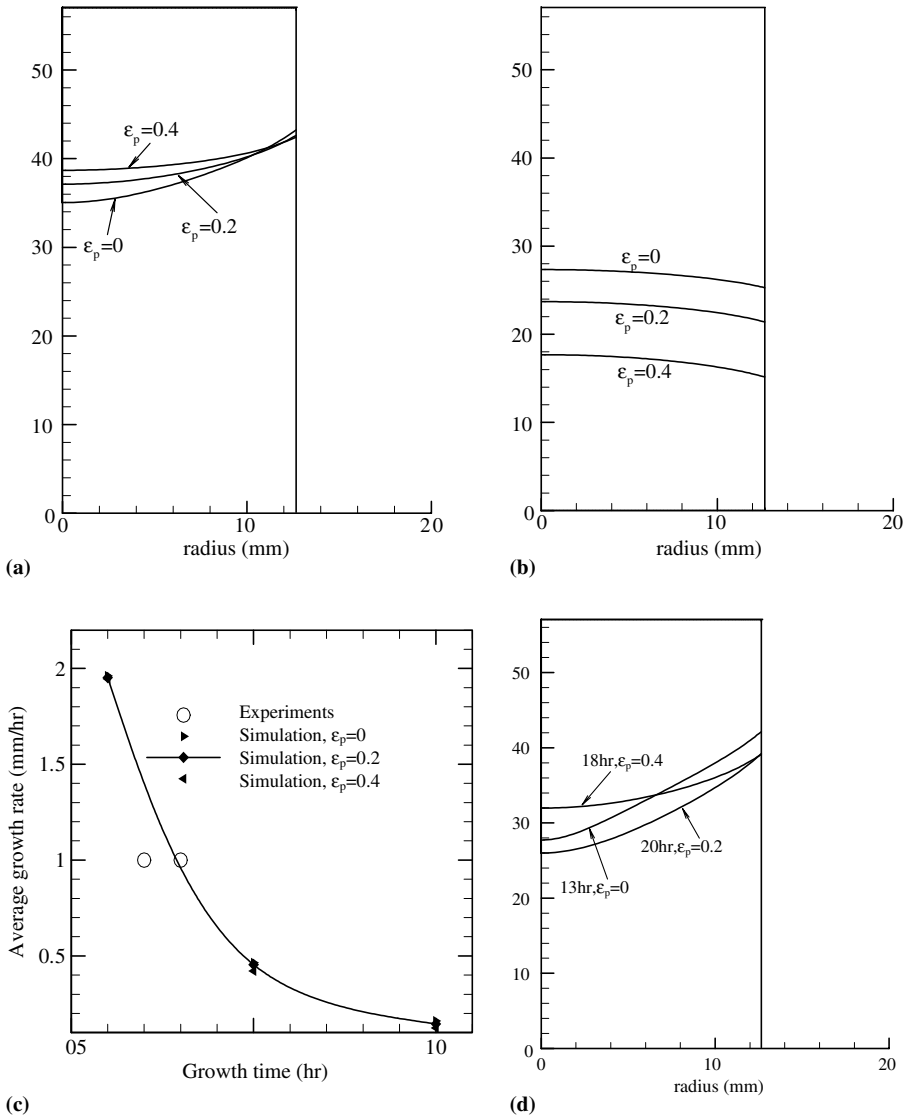

Fig. 8. (a) Crystal interface shapes after 10 h; (b) source top surface shapes after 10 h and (c) variations of the growth rate at different porosities. Experimental data are obtained from NCSU and (d) Crystal interface shapes at the end of growth process.

References

[1] J.C. Rojo, L.J. Schowalter, R. Gaska, M. Shur, M.A. Khan, J. Yang, D.D. Doleske, Growth and characterization of epitaxial layers on aluminum nitride substrates prepared for bulk single crystals, J. Cryst. Growth 240 (2002) 508–512.

[2] L. Liu, J.H. Edgar, Substrates for gallium nitride epitaxy, Mater. Sci. Eng. R 37 (2002) 61–127.

[3] J.C. Rojo, G.A. Slack, K. Morgan, B. Raghothamachar, M. Dudley, L.J. Schowalter, Report on the growth of bulk aluminum nitride and subsequent substrate preparation, J. Cryst. Growth 231 (2001) 317–321.

[4] A.S. Segal, S.Yu. Karpov, Yu.N. Makarov, E.N. Mokhov, A.D. Roenkov, M.G. Ramm, Yu.A. Vodakov, On mechanisms of sublimation growth of AlN bulk crystals, J. Cryst. Growth 211 (2000) 68–72.

[5] G.A. Slack, Growth of AlN single crystals, Mater. Res. Soc. Symp. Proc. 512 (1998) 35–40.

[6] N.B. Singh, A. Berghmans, H. Zhang, T. Wait, R.C. Clarke, J. Zingaro, J.C. Golombeck, Physical vapor transport growth of large AlN crystals, J. Cryst. Growth 250 (2003) 107–112.

[7] B. Raghothamachar, M. Dudley, J.C. Rojo, K. Morgan, L.J. Schowalter, X-ray characterization of bulk AlN single crystals grown by the sublimation technique, J. Cryst. Growth 250 (2003) 244–250.

[8] K.L. Choy, Chemical vapor deposition of coatings, Prog. Mater. Sci. 48 (2003) 57–170.
[9] R.L. Mahajan, Transport Phenomena in Chemical Vapor-Deposition Systems, Advanced in Heat Transfer, 28, Academic Press, New York, 1996, 339–425.
[10] G. Evans, R. Greif, A two-dimensional model of the chemical vapor deposition of silicon nitride in a low-pressure hot-wall reactor including multicomponent diffusion, Int. J. Heat Mass Transfer 37 (1994) 1535–1543.
[11] P.O. Iwanik, W.K.S. Chiu, Temperature distribution of an optical fiber traversing through a chemical vapor deposition reactor, Numer. Heat Transfer A-Appl. 43 (2003) 221–237.
[12] H. Yoo, Y. Jaluria, Thermal aspects in the continuous chemical vapor deposition of silicon, J. Heat Trans.-Trans. ASME 124 (2002) 938–946.
[13] O. Klein, P. Philip, Transient temperature phenomena during sublimation growth of silicon carbide single crystals, J. Cryst. Growth 249 (2003) 514–522.
[14] S. Fujiwara, Y. Namikawa, T. Kotani, Growth of 1 in. diameter ZnSe single crystal by the rotational chemical vapor transport method, J. Cryst. Growth 225 (1999) 43–49.
[15] L. Liu, J.H. Edgar, Transport effects in the sublimation growth of aluminum nitride, J. Cryst. Growth 220 (2000) 243–253.
[16] R.-H. Ma, H. Zhang, S. Ha, M. Skowronski, Integrated process modeling and experimental validation of silicon carbide sublimation growth, J. Cryst. Growth 252 (2003) 523–537.
[17] R.-H. Ma, H. Zhang, V. Prasad, M. Dudley, Growth kinetics and thermal stress in the sublimation growth of silicon carbide, Cryst. Growth Des. 2 (2002) 213–220.
[18] M. Kaviany, Principles of Heat Transfer in porous Media, Springer, New York, 1995.
[19] Q.-S. Chen, H. Zhang, V. Prasad, C.M. Balkas, N.K. Yushin, Modeling of heat transfer and kinetics of physical vapor transport growth of silicon carbide crystals, J. Heat Trans.—Trans. ASME 123 (2001) 1098–1109.
[20] M.F. Modest, Radiative Heat Transfer, McGraw-Hill, New York, 1993.
[21] B. Wu, R.-H. Ma, H. Zhang, M. Dudley, R. Schlesser, Z. Sitar, Growth kinetics and thermal stress in AlN bulk crystal growth, J. Cryst. Growth 253 (2003) 326–339.
[22] M.V. Averyanova, I.N. Przhevalskii, S.Yu. Karpov, Yu.N. Makarov, M.S. Ramm, R.A. Talalaev, Analysis of vaporization kinetics of group-III nitrides, Mater. Sci. Eng. B 43 (1997) 167–171.
[23] Y.A. Cengel, Heat Transfer, Second ed., McGraw-Hill, New York, 2003.